ACS Catalysis

pubs.acs.org/acscatalysis

Research Article

Unraveling Electroreductive Mechanisms of Biomass-Derived Aldehydes via Tailoring Interfacial Environments

Hengzhou Liu, Deep M. Patel, Yifu Chen, Jungkuk Lee, Ting-Han Lee, Sarah D. Cady, Eric W. Cochran, Luke T. Roling,* and Wenzhen Li*

Cite This: *ACS Catal.* 2022, 12, 14072−14085

Read Online

ACCESS | Metrics & More | Article Recommendations | Supporting Information

ABSTRACT: Electrochemical reduction of biomass-derived feedstocks holds great promise to produce value-added chemicals or fuels driven by renewable electricity. However, mechanistic understanding of the aldehyde reduction toward valuable products at the molecular level within the interfacial regions is still lacking. Herein, through tailoring the local environments, including H/D composition and local H_3O^+ and H_2O content, we studied the furfural reduction on Pb electrodes under acid conditions and elucidated the pathways toward three key products: furfuryl alcohol (FA), 2-methylfuran (MF), and hydrofuroin. By combining isotopic labeling and incorporation studies, we revealed that the source of protons (H_2O and H_3O^+) plays a critical role in the hydrogenation and hydrogenolysis pathways toward FA and MF, respectively. In particular, the product-selective kinetic isotopic effect of H/D and the surface-property-dependent hydrogenation/deuteration pathway strongly impacted the generation of FA but not MF, owing to their different rate-determining steps. Electrokinetic studies further suggested Langmuir−Hinshelwood and Eley−Rideal pathways in the formation of FA and MF, respectively. Through modifying the double layer by cations with large radii, we further correlated the product selectivity (FA and MF) with interfacial environments (local H_3O^+ and H_2O contents, interfacial electric field, and differential capacitances). Finally, experimental and computational investigations suggested competitive pathways toward hydrofuroin and FA: hydrofuroin is favorably produced in the electrolyte through the self-coupling of ketyl radicals, which are formed from outer-sphere, single-electron transfer, while FA is generated from hydrogenation of the adsorbed furfural/ketyl radical on the electrode surface.

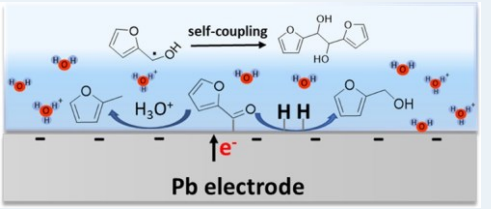

KEYWORDS: *biomass-derived aldehyde, electrocatalytic hydrogenation, pathway, selectivity, outer-sphere, interfacial environments*

INTRODUCTION

Electrocatalytic hydrogenation (ECH) provides a sustainable and environmentally friendly approach to produce chemicals and biofuels by operating under mild conditions with "clean" electrons as the reducing agents, instead of dealing with fossil-derived H_2 at elevated temperature/pressure.[1−3] ECH of biomass-derived compounds, such as furfural and 5-hydroxymethylfurfural (HMF), is regarded as an attractive approach to produce valuable chemicals and fuels.[4,5] Specifically, furfural as a platform aldehyde chemical has already exceeded a productivity of 400 ktons per year.[1] Its hydrogenation products, furfuryl alcohol (FA) and 2-methylfuran (MF), have wide applications in polymer and biofuel industries.[6,7] Its C−C bond dimerization product, hydrofuroin, holds great promise to produce fuel precursors.[8,9]

In the past few years, research efforts have been dedicated to exploring electrocatalysts and/or processes to improve the selectivity toward a target product and increase its energy efficiency.[9−13] However, mechanistic understanding of electrochemistry in aldehyde transformation, through ECH of furfural as a model reaction, remains insufficient. Our previous study has distinguished the ECH pathway toward alcohol/alkyl (i.e., FA/MF) and the direct outer-sphere pathway toward dimeric (i.e., hydrofuroin) products on Cu electrodes[14] and highlighted the vital role of adsorption of hydrogen in their production rates and selectivity. However, it still lacks molecular-level mechanistic information on the changes in product selectivity at the electrode/electrolyte interface with sophisticated chemical and physical properties. Specific questions remaining unclear so far include: Are both furfural and hydrogen chemically bonded to the catalyst surface during the formation of FA and MF? What is the crucial difference governing the hydrogenation and hydrogenolysis pathways toward these two products, and how do the local chemical and physical environments influence the reductive pathways? In addition, most studies have been empirical and given inconsistent explanations on the formation of hydrofuroin, which needs to be clearly elucidated. Some works suggested that hydrofuroin is formed via electron tunneling[14,15] with neither reactant nor

Received: June 30, 2022
Revised: October 15, 2022

https://doi.org/10.1021/acscatal.2c03163
ACS Catal. 2022, 12, 14072−14085

product adsorbed[16] and thus is independent of the types of electrodes and insensitive to their surface properties, while other studies contended that hydrofuroin and FA might share a common intermediate—ketyl radicals,[9,17] and the formation of hydrofuroin is a complete surface reaction through C−C coupling of these radical adsorbates on the electrode.[18] However, no direct experimental or theoretical evidence has yet been provided. Therefore, the true reduction pathway toward hydrofuroin, whether it is a complete surface reaction, a fully outer-sphere (nonsurface) step, or a combined process, is still under debate. The relation between the formation of hydrofuroin and other products (i.e., FA) has also been largely uninvestigated. All of these questions have motivated a deeper study in this work to systematically understand the reaction mechanisms using furfural as a model compound.

Since understanding the mechanisms of ECH of furfural (a C5 organic compound) is challenging due to numerous sensitive and influential selectivity-determining factors and multiple transformation pathways, as well as the complexity of the electrode/electrolyte interface,[19] combining scientific methods and research tools is needed to examine the reaction mechanisms, rather than through investigating a single chosen parameter (e.g., half-cell potentials, electrolyte pH). For instance, incorporating isotopes into unsaturated bonds is able to help acquire new understandings of electrochemical reactions,[20] such as CO_2 reduction,[21−24] water oxidation,[25] O_2 reduction,[26] and N_2 reduction.[27] In addition, through tailoring the electrode double layer and varying its chemical or physical properties, such as thickness and differential capacitance,[28,29] local pH,[30−32] interfacial electric field,[33,34] or binding of certain intermediate species,[32,35] the reaction activity and product selectivity are altered, and therefore, the mechanistic information at the electrode−electrolyte interface could be obtained. However, these methods/techniques were rarely reported to elucidate the electrochemical reaction mechanisms of biomass-derived molecules.

Herein, we seek to unravel sophisticated electrochemistry associated with furfural reduction under acidic conditions by tailoring the interfacial environments. Electrochemical studies were conducted on Pb electrodes based on their observed potential-dependent pathways toward four key products: FA, MF, hydrofuroin (Scheme 1), and H_2 (produced from hydrogen evolution reaction, HER). H/D kinetic isotopic effect (KIE) and isotopic incorporation studies were used first to distinguish different roles of protons (from H_3O^+ and H_2O) in the rate-determining step (RDS) for the formation of FA and MF. Specifically, the pathway toward FA showed a strong KIE in its production rate, as well as incorporation-selective and surface-property-dependent H/D additions. In contrast, the formation of MF did not show such notable H/D preferences. Combining with electrokinetic studies, we found that FA is formed through surface reactions following the Langmuir−Hinshelwood (L−H) mechanism, while MF is generated via an interfacial Eley−Rideal (E−R) route. Furthermore, through tailoring the electrochemical double layer using a series of quaternary alkyl ammonium cations, the relationship between the microenvironments at the interfacial regions and the product selectivity was established. Finally, electron paramagnetic resonance (EPR) spectroscopy and density functional theory (DFT) calculations suggested that hydrofuroin is formed via the radical−radical self-coupling in the solution, in which the radical is likely generated from an outer-sphere process. The acquired mechanistic insights and methods from this work on electrochemical reduction of the aldehyde group in furfural to alcohol, alkyl, and dimer species could be extended to other organic compounds with carbonyl groups, such as 5-hydromethylfurfural (HMF) and benzaldehyde.

Scheme 1. Key Products from Electroreduction of Furfural

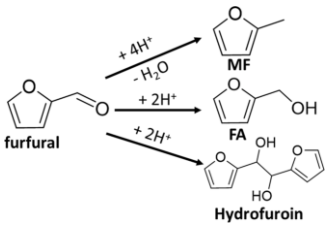

RESULTS AND DISCUSSION

Potential-Dependent Selectivity on Pb with Product-Selective KIE. Pb electrodes are known with large binding energy differences among different adsorbates (including reactants, intermediates, products), particularly aldehyde and hydrogen.[14,18] This suggested that a large overpotential difference is required to perform ECH and HER, with potential-dependent selectivity to the major products (i.e., FA, MF, hydrofuroin, and H_2), which can help decouple the key parameters for separately investigating reaction pathways.

We first performed linear sweep voltammetry (LSV) in the electrolyte (0.5 M H_2SO_4 in 1:3 (v/v) CH_3CN/H_2O cosolvent) with and without furfural. As shown in Figure 1a, with the addition of 50 mM furfural (blue curve), the onset potential (defined as the potential at -1 mA cm^{-2}) on Pb foil was positively shifted around 150 mV to -0.55 V_{RHE} (V_{RHE}/V vs RHE, hereinafter), as compared to the result without furfural (red curve). In the potential region of -0.75 to -0.85 V_{RHE} on the blue curve, a flat current density was observed, suggesting that greater adsorption energy was required to adsorb certain furanic intermediates. At potentials <-0.85 V_{RHE}, the current density of HER (red curve) outperformed that of furfural reduction (blue curve), indicating that the addition of furfural suppresses the activities of both ECH and HER. These results suggested the competitive adsorption between aldehyde and H on the Pb surface, particularly at high current densities with gradually saturated active sites. A Nyquist plot obtained from EIS further supported this competing adsorption relation on the Pb surface (Figure S2).

Since large binding energy differences among different adsorbates and various pathways exist on the Pb electrode, a potential-dependent selectivity toward the major products (FA, MF, hydrofuroin, and H_2) would be expected. Indeed, 1 h chronoamperometry (CA) tests (Figure 1b) clearly showed hydrofuroin as the dominant product (~30% FE) in the less negative potential region from -0.55 to -0.85 V_{RHE}, with small amounts of FA and MF (FE: <5%). In contrast, at potentials more negative than -1.00 V_{RHE}, an opposite product distribution was observed. In particular, the formation of MF, FA, and H_2 dominated at -1.20 V_{RHE}, resulting in their FE of 18.5, 29.0, and 15.9%, respectively, with hydrofuroin minimized to 7.1%. The increase in FE of FA and MF is in line with the increase of H_2 when negatively shifting the potential from -0.65 V_{RHE}, which agreed well with our prior studies that ECH and HER on Cu electrodes shared the common intermediate H_{ads}, and its high coverage is necessary

https://doi.org/10.1021/acscatal.2c03163
ACS Catal. 2022, 12, 14072−14085

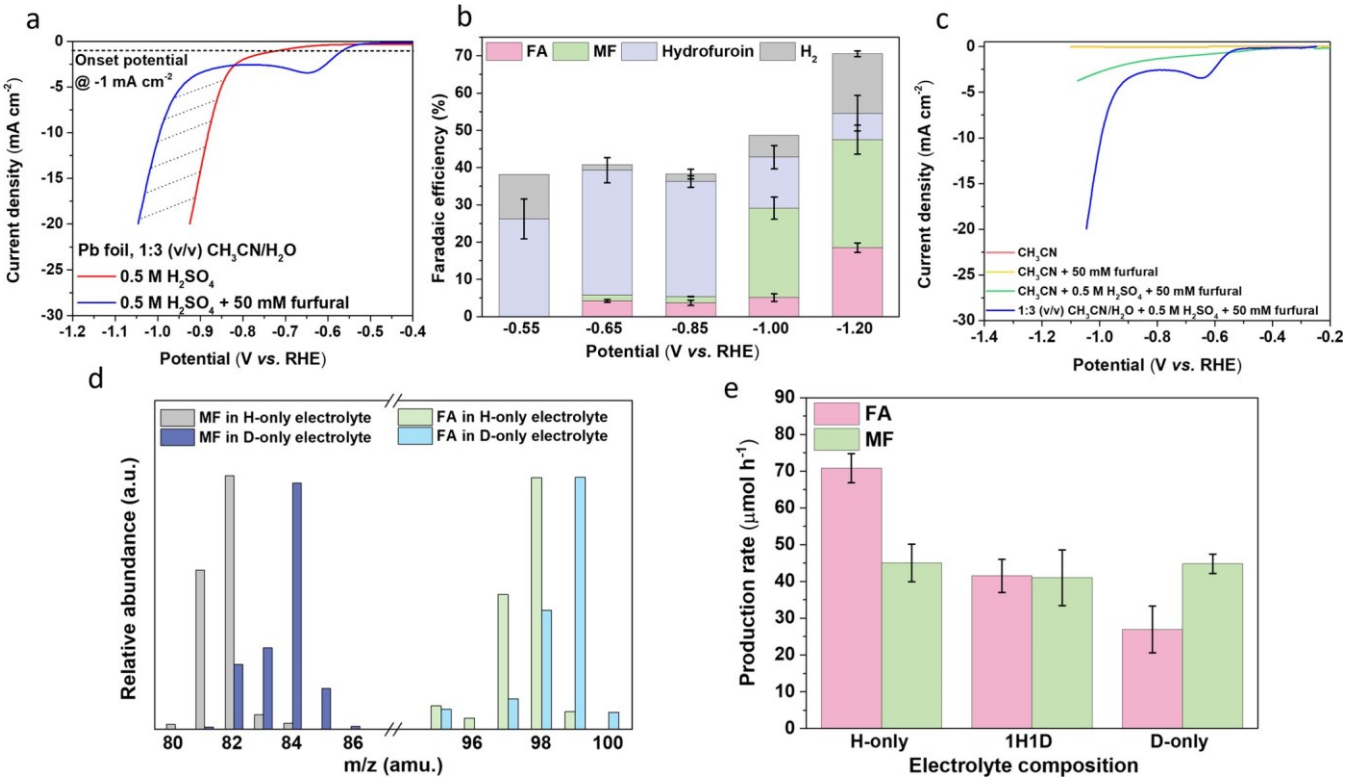

Figure 1. ECH of furfural under acid conditions on Pb electrodes. (a) LSV curves on Pb foil with (blue curve) or without (red curve) 50 mM furfural. (b) Faradaic efficiency of ECH at different applied potentials for 1 h electrolysis with 20 mM furfural. Furfural was dissolved in 1:3 (v/v) CH_3CN/H_2O cosolvent with 0.5 M H_2SO_4. (c) LSV curves on Pb foil in four solutions with varied compositions. (d) Mass spectra of MF and FA produced from 1 h electrolysis on Pb foil at −1.20 V_{RHE} in H-only and D-only electrolytes. (e) Production rate of FA and MF for 1 h electrolysis on Pb foil at −1.20 V_{RHE} in three electrolytes with varying H/D compositions. H-only, D-only, and 1H1D electrolyte represent 20 mM furfural in 1:3 (v/v) CH_3CN/H_2O with 0.5 M H_2SO_4, in 1:3 (v/v) CD_3CN/D_2O with 0.5 M D_2SO_4, and their mixtures with a volumetric ratio of 1:1, respectively. The geometric area of the electrode was 6 cm^2 for −0.55 and −0.65 V_{RHE} and 2 cm^2 for all other conditions.

for both ECH and HER products.[14] Note that the unbalanced charge from CA measurements likely resulted from side reactions to large molecular oligomers (e.g., humins) or decomposition products during electrolysis in the acidic electrolyte,[18,36] and our observed charge balance is consistent with previous studies under similar conditions.[14,36,37] In addition, furfural reduction to FA and MF on Pb electrodes followed a parallel pathway, supported by the negligible MF formation through the electrolysis of FA at −1.20 V_{RHE} for 3 h (Figure S3), which is in line with our previous work.[14] This indicated that once FA (from furfural reduction) is desorbed from the surface, it does not undergo further reduction. In other words, FA is not an intermediate to MF.

The impact of water on furfural reduction was first analyzed by LSV by considering alternative CH_3CN-based solutions with varied proton contents. Figure 1c shows that a considerable current density was only observed in the presence of sufficient H_2O. The m/z signal (Figure 1d) from gas chromatography−mass spectrometry (GC-MS) in the range of 80 to 84 and 95 to 99 corresponds to the fragment pattern of MF and FA, respectively. Through 1 h electrolysis of 20 mM furfural at −1.20 V_{RHE}, when the electrolyte was switched from H-only [i.e., 0.5 M H_2SO_4 in 1:3 (v/v) CH_3CN/H_2O cosolvent, hereinafter] to D-only [i.e., 0.5 M D_2SO_4 in 1:3 (v/v) CD_3CN/D_2O cosolvent, hereinafter], the predominant ion peaks of FA and MF all shifted to higher m/z values, indicating that the concentration of protons is critical to the furfural reduction. Control experiments under various H/D compositions of electrolytes have excluded the proton sources from CH_3CN (Tables S1−S5). It is worth noting that it is hard to experimentally differentiate proton sources from water or acid using isotopes because of the fast equilibrium between acid and water protons. Nuclear magnetic resonance (NMR) results agreed well with GC-MS to exclude CH_3CN as the proton source; meanwhile, it identified the H/D positions in the products (details shown in Figures S5−S13). Based on the ^{1}H-NMR test results in Figures S5−S12, FA is formed by adding one H/D to the hydroxyl group and the other to the carbonyl carbon. MF is produced by adding both H/D to the alkyl group followed by C-O scission to remove one H_2O/D_2O molecule (Figure S13).

Besides tracking proton sources from isotopic labeling, the H/D kinetic isotope effect (KIE) study is a vital tool to investigate reaction mechanisms when there is a proton or H involved in the bond breaking via the change of the zero-point energy of the ground vibrational state.[20] Herein, we conducted 1 h CA measurements in the electrolyte of H-only, D-only, and H-D mixture with a volumetric ratio of 1:1 (denoted as 1H1D, hereinafter) on Pb foil. We kept the same acidity (the same concentration of 0.5 M H_2SO_4 or D_2SO_4) but with varying H/D ratios in the electrolytes. The LSV and current density−time profiles (Figure S14a) showed a decreased reaction rate when the electrolyte was gradually deuterated, suggesting a decrease in the furfural reduction activity. The LSV profiles of HER (Figure S14c) showed a similar decrease trend as the gradual change of electrolyte composition, which indicated that ECH

https://doi.org/10.1021/acscatal.2c03163
ACS Catal. 2022, 12, 14072−14085

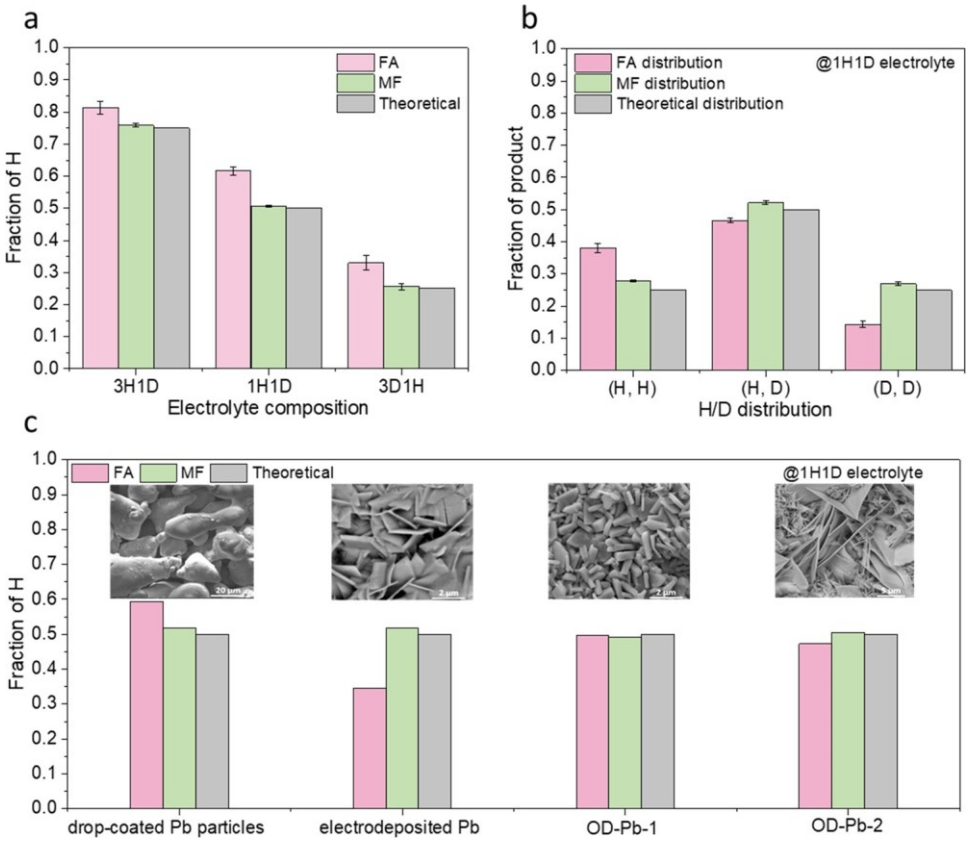

Figure 2. H/D isotopic compositions and distributions in products FA and MF. (a) The fraction of H and (b) H/D distribution in the products after electrolysis and their theoretical values in the electrolyte with different compositions. The electrolysis was performed on Pb foil at −1.20 V_{RHE} for 1 h. The electrolyte was prepared in 0.5 M H_2SO_4 with 1:3 (v/v) CH_3CN/H_2O cosolvent and 20 mM furfural. 3H1D, 1H1D, and 3D1H electrolytes represent the volumetric ratios between hydrogenated and deuterated solutions are 3:1, 1:1, and 1:3, respectively. (c) H/D distribution in the products and their theoretical values on different Pb-based electrodes. The electrolysis was performed in 1H1D electrolyte at −1.20 V_{RHE} for 1 h. The inset showed the SEM images of these four Pb-based electrodes.

and HER shared the common Volmer steps. Through analyzing product distributions for furfural reduction, as shown in Figure 1e, the production rate of FA was gradually decreased from 70.8 to 26.5 μmol h^{-1} (~2.7 times lower) by continuously increasing the ratio of D in the electrolyte; in contrast, MF was maintained from 38.5 to 45.0 μmol h^{-1} (~1.2 times higher). That is, with a controlled acidity, a product-selective KIE was only observed in the formation of FA: A more favorable pathway toward FA was obtained in the electrolyte with a higher ratio of H/D, whereas the H/D isotope effect did not influence furfural-to-MF conversion. This product-selective KIE suggests possibly different roles of H_2O and acidity (i.e., H_3O^+) in the RDS of FA and MF productions. The FA formation involved the proton or hydrogen transfer in the RDS, while the transfer of protons in the bulk electrolyte was not a part of the RDS in the hydrogenolysis pathway for MF generation.

Hydrogen/Deuterium Isotopic Incorporations for Distinguishing FA and MF Pathways. If the above-observed product-selective KIE is due to transport effects, e.g., lower flux of deuterium (relative to hydrogen) from the bulk solution to the Pb electrode surface, or lower surface diffusion of deuterium to the adjacent regions of adsorbed furfural, isotopic incorporation can provide molecular-level information on how H/D atoms are selectively added to the unsaturated bonds without dealing with these transport issues. Furfural reduction on Pb foil was conducted at −1.20 V_{RHE} for 1 h with varying H/D ratios of 1:3, 1:1, and 3:1, denoted as 1H3D, 1H1D, and 3H1D, respectively. The isotope composition, specifically the fraction of D (f_D) and H (f_H) in the products, was calculated by solving the following two binary linear equations quantitatively obtained from GC-MS, with details shown in Supporting information note 2.

$$S_a = f_H \times S_{Ha} + f_D \times S_{Da}$$

$$S_b = f_H \times S_{Hb} + f_D \times S_{Db}$$

where S_a and S_b represent the relative abundance of MS signals of products at an m/z ratio of a and b, respectively. Similarly, S_{Ha} and S_{Hb}, and S_{Da} and S_{Db} correspond to the relative abundance of products at the same m/z ratios after electrolysis of H-only and D-only electrolyte with 20 mM furfural, respectively.

As shown in Figure 2a, the f_H in FA is 0.81, 0.62, and 0.33 in the electrolyte of 3H1D, 1H1D, and 3D1H, respectively, consistently higher than the theoretical values of 0.75, 0.50, and 0.25. In contrast, the respective f_H values in MF, i.e., 0.76, 0.26, and 0.51, are close to the correspondingly theoretical values. Regardless of electrolyte pH (H_2SO_4/D_2SO_4 concentration from 0.25 to 0.75 M, Figure S15a) and cathodic potentials (from −1.10 to −1.30 V_{RHE}, Figure S15b), the large difference of f_H between FA and MF and the consistently higher f_H in FA than theoretical values (i.e., 0.5, in the 1H1D electrolyte) are maintained. A series of control experiments

https://doi.org/10.1021/acscatal.2c03163
ACS Catal. 2022, 12, 14072−14085

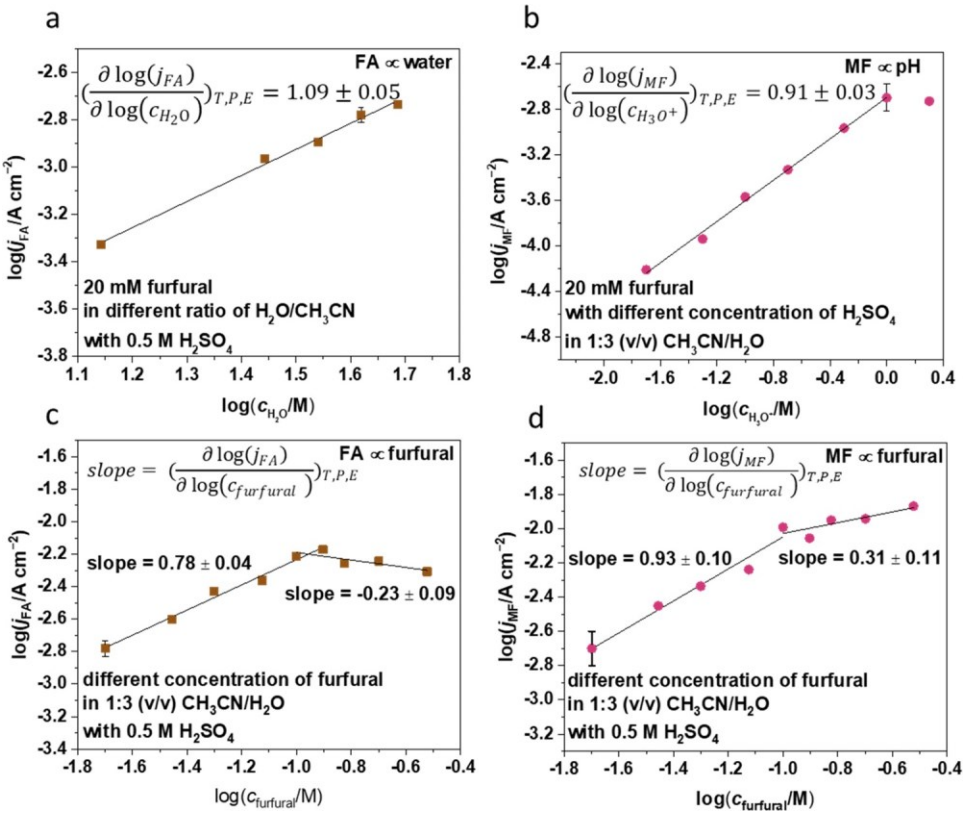

Figure 3. Electrokinetic studies for ECH of furfural on Pb foil. (a) Dependence of partial current density of FA on H_2O concentration. (b) Dependence of partial current density of MF on H_3O^+ concentration. To adjust electrolyte pH in (b) while maintaining a constant ionic strength at 0.5 M, different ratios of H_2SO_4/Na_2SO_4 were used. Dependence of partial current densities of (c) FA and (d) MF on furfural concentration. The electrolysis was performed on Pb foil at −1.20 V_{SHE} with the applied charge of 60 C.

have excluded the H−D exchange between reactant/products and solvents (water and acetonitrile) and acid-catalyzed Cannizzaro-type disproportionation reactions (as no furoic acid was detected) during the 1 h tests (Supporting information note 2).

Further analysis of the H/D distribution in MF and FA was obtained by substitution of f_H and f_D to binomial distribution equations, with details shown in Supporting information note 2. Figure 2b shows that the H/D distribution in MF approached the theoretical values of 0.25, 0.50, and 0.25 for (H, H), (H, D), and (D, D) products, respectively. Owing to the large f_H in FA, H/D distributions in FA appeared largely deviated from that in MF and the corresponding theoretical values. As such, a higher fraction of (H, H) product (0.38) and a lower fraction of (D, D) product (0.14) were observed, as compared to their theoretical value of 0.25. Similar large deviations were also observed in the electrolytes with other H/D ratios (i.e., 3H1D, 3D1H, Figure S16).

Then, we modified the surface of Pb electrodes and carried out isotopic labeling tests on them. Four Pb-based electrodes were prepared from different methods, denoted as follows: (i) drop-coated micrometer-sized Pb, (ii) electrodeposited Pb, and oxide-derived Pb prepared (iii) in strong acid (OD-Pb-1) and (iv) in base (OD-Pb-2). Various characterizations, including SEM images, double-layer capacitance, and XRD, confirmed their differences in morphologies, active surface areas, and Pb phases, respectively (see Figures S17−20 for details). The isotopic experiments were then conducted in the 1H1D electrolyte at −1.20 V_{RHE} for 1 h. As shown in Figure 2c, a large difference in f_H in FA, ranging from 0.34 to 0.59, was observed on these four Pb electrodes, significantly deviating from the constant value of 0.62 on Pb foil at the same test condition. In contrast, the f_H close to the theoretical value (i.e., ∼0.5) was kept nearly constant in MF on all four Pb-based electrodes, consisting with the value on Pb foil.

Based on isotopic incorporation results on different Pb-based electrodes, we proposed that the H/D distribution difference in FA and MF could be attributed to their different RDS for H/D additions. For example, the RDS for FA formations could be the proton/deuterium reduction to adsorbed H/D on the surface; the higher f_H in FA is because the adsorption of H is more favored than D at identical potential and vice versa, resulting from their different binding energy or kinetic isotopic effects of H/D.[19] These different preferences for H/D bindings depend on the structures and/or the electronic properties of the electrode surface. In contrast, the formation of MF does not exhibit any KIE since proton transfer followed by the hydrogenolysis of the C−O bond did not participate in the RDS. As such, when the ratio of H in the electrolyte is fixed, its fraction in the product MF should remain constant (as we observed experimentally). Despite how catalyst structures govern the selective formation of FA is worth further studies, isotopic results suggested that protons indeed play different roles in the formation of FA and MF, which are unlikely to share the same selectivity-determining intermediates. The following section further investigated detailed differences between furfural reductive pathways toward FA and MF.

Electrokinetics in Elucidating FA and MF Pathways. Electrokinetic studies were employed to further study the

https://doi.org/10.1021/acscatal.2c03163
ACS Catal. 2022, 12, 14072−14085

critical role of protons in the reduction pathways toward FA and MF. Electrokinetic fittings were all determined from CA at −1.20 V at the SHE scale (−1.20 V_{SHE}) with the same amount of charge (i.e., 60 C) supplied. The reaction order dependence was obtained by fitting the partial current density against the concentration of each substrate on a log−log scale.

As shown in Figure 3a, by varying the volume percentage of H_2O in the cosolvent from 25 to 87.5% (i.e., the molar concentration of H_2O in the range of 13.6−48.6 M), it is interesting to observe a slope of 1.09, suggesting a first-order dependence of the furfural-to-FA reaction and emphasizing that the H_2O content is critical to produce FA. In the same range, a negative reaction order (i.e., −0.28, Figure S21a) was observed for the furfural-to-MF reaction, suggesting that MF is suppressed with increased H_2O content, which could be due to the increased FA production occupied some of the active sites that were expected to be used for MF. It is noted that the solvent CH_3CN has been confirmed nonreactive to provide the proton source for ECH of furfural in our conditions, so the water content can be adjusted by changing the cosolvent ratio. In comparison, the furfural-to-MF reaction is highly dependent on the acidity of the electrolyte. Figure 3b shows a reaction order of 0.91 via adjusting the H_3O^+ concentration from 0.02 to 1 M. In contrast, a declining tendency to FA (i.e., reaction order of −0.32, Figure S21b) was obtained. That is, in the pH range of 0−1.7, an opposite trend of FA and MF was observed. Apparently, the pathway toward MF is energetically more favorable in the more acidic electrolyte, which suggested that furfural would be protonated, or hydronium is involved in the MF formation pathway because Brønsted or Lewis acids are well known to interact with oxygen moieties in the C−O bonds of many substrates to lower their activation barriers for subsequent C−O scission.[38−40] The slightly decreased partial current density toward FA indicated that hydronium is not directly involved in the reaction pathway until after the rate-determining step (RDS).

In a similar way, proton-involved C−O cleavage can be extended to other furan-based aldehyde compounds, i.e., HMF and 5-methylfurfural (5-MF), in the strongly acidic solution (0.5 M H_2SO_4). The hydrogenolysis of HMF was observed on the Ag electrode (Figure S22) that led to the formation of 5-methylfurfural (5-MF) and 2,5-dimethylfuran (DMF). With 5-MF as the reactant under identical electrolytic conditions, DMF was also obtained as a dominant product. In addition, the H_3O^+ concentration-dependent hydrogenolysis rates for HMF and 5-MF are maintained and agreed with the furfural-to-MF reaction (Figure S22). Similar to the relationship between FA and MF from furfural reduction, the opposite trend between alcohol product 2,5-bis(hydroxymethyl)furan (BHMF) and alkyl product DMF was also observed from HMF electroreduction by varying H_3O^+ concentration.

We further decreased H_3O^+ concentration and performed LSV and CA tests for ECH of furfural in pH 3−11 buffer solutions (Figure S23). As expected, MF was no longer produced, and FA became a dominant product (especially at more negative potentials). These electrokinetic results separately studied the different roles of H_2O and H_3O^+ in FA and MF formation pathways. The different pH dependence between FA and MF formations in the SHE scales suggested with the adsorbed furfural. In comparison, the highly selective production of FA in solutions with sufficient H_2O is consistent with the product-selective KIE, which suggested a different RDS for FA generation, such as the dissociation of H_2O for the following adsorption of H on the surface.

Based on the above understanding of the role of protons involved in the FA and MF formation pathways, it enables the optimization of the electrolyte composition, achieving the FA selectivity of 89% without MF production on Pb foil in pH 7 electrolyte (Figure S23). If we substitute Pb foil with a high-surface-area OD-Pb-2 electrode (Figure S24), the FA selectivity can be further increased to >99% with the same electrolyte composition. It is worth noting that the FE of FA and H_2 consistently increased by negatively shifting the cathodic potentials, indicating that ECH and HER shared the same Volmer step.

To further test how H_2O and H_3O^+ are involved in their distinct reduction pathways, the reaction order dependence of FA and MF on furfural concentration was analyzed. When we varied furfural concentration in a wide range (Figure 3c), the ECH rate to FA initially exhibited a reaction order of 0.78 in its lower concentrations (from 0.02 to 0.1 M), followed by a slightly negative order at high concentrations (>0.1 M). This result suggests that the furfural or H at their high coverage (at strongly negative potentials lower than −1.20 V_{SHE}) might compete for the active sites. In contrast, furfural-to-MF conversion (Figure 3d) in the same two regions followed positive reaction orders (i.e., 0.93 and 0.31). We derived rate expressions for possible reaction mechanisms and related them to the kinetic results (detailed derivations are shown in the Supporting information note 3).[41] The switch of reaction order from positive to negative for the furfural-to-FA reaction suggests an L−H mechanism with competitive adsorption of furfural and H. In comparison, both positive orders for the furfural-to-MF reaction in these two concentration regions further suggested an E−R mechanism, which requires the adsorbed furfural to couple with protons at the near-surface electrolyte. That is, under acidic conditions and strongly negative potentials, the E−R mechanism suggested that the kinetics for MF formation is largely limited by furfural, not H coverage on the surface.[41−43] A simplified scheme is described in Figure S25 to distinguish these two pathways. It should note that the reaction order dropped to 0.31 (not being kept at 1) for MF in the high furfural concentration region may be due to the saturation of active sites for furfural adsorption (internal mass transport limitation), the diffusion limitation of protons to the near-surface electrolyte (external mass transfer limitation), or not all four protons participated into the E−R route for MF formation.

Tafel slopes (Figure S21c,d) of 160 (for FA) and 175 (for MF) mV dec^{-1} corresponded to an empirical transfer coefficient [$\alpha = 2.303RT/F \times d\log(j)/dE$] of 0.37 and 0.34, respectively, strongly suggesting that their kinetics is limited by the initial one-electron transfer. These electrokinetic studies collectively suggested the rate laws for FA and MF as follows

$$i_{FA} \propto C_{H_2O}^{1.09} \times C_{furfural}^{0.78} \times \exp\left(\frac{F}{\eta}\right)$$

$$i_{MF} \propto C_{H_3O}^{0.91} \times C_{furfural}^{0.93} \times \exp\left(\frac{F\eta}{2.94RT}\right) \times \exp\left(\frac{F}{2.70RT}\right)$$

https://doi.org/10.1021/acscatal.2c03163
ACS Catal. 2022, 12, 14072−14085

that they do not share the same reaction pathways or RDS. In particular, the highly pH-dependent MF generation suggested that its formation follows an E−R mechanism, in which highly concentrated H_3O^+ in solution directly attacked and coupled

where F is the Faraday constant, η is the overpotential, R is the ideal gas constant, T is the normal temperature, and C is the

https://doi.org/10.1021/acscatal.2c03163
ACS Catal. 2022, 12, 14072−14085

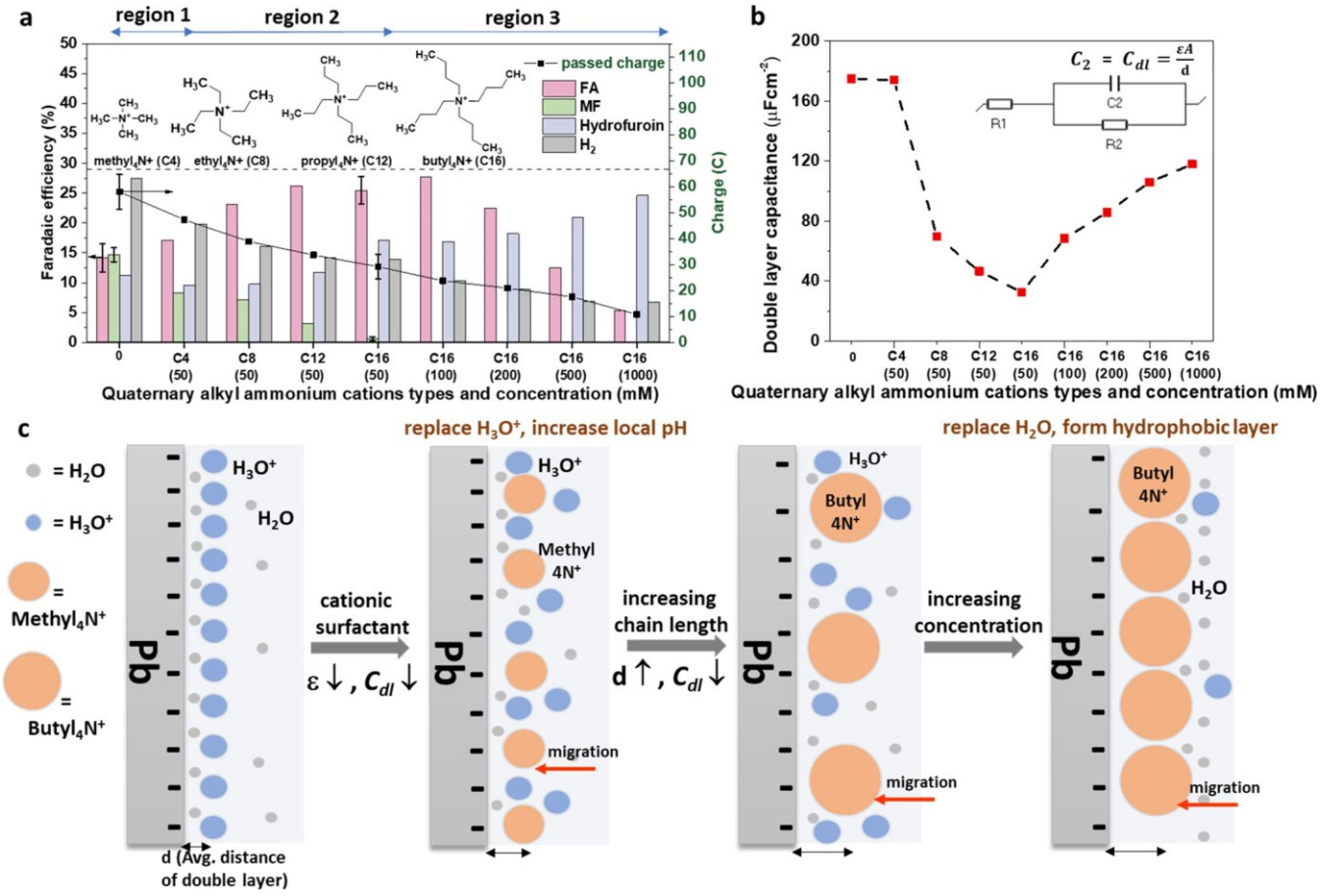

Figure 4. Tailoring the electrochemical double layer of Pb electrode by quaternary alkyl ammonium cations. (a) Faradaic efficiency (left y-axis) and passed charges (right *y*-axis) and (b) double-layer capacitance of ECH with different types and concentrations of quaternary alkyl ammonium cations. The inset in panel (a) shows the chemical structure of quaternary alkyl ammonium cations of methyl$_4$N+ (C4), ethyl$_4$N+ (C8), propyl$_4$N+ (C12), and butyl$_4$N+ (C16). The tick labels on the *x*-axis in panels (a) and (b) showed various types of cations from C4 to C16, and the values in the bracket are their concentrations. The inset in panel (b) shows the equivalent circuit of the double layer and the formula of double-layer capacitance. (c) Proposed interfacial structure changes after being modified by cationic surfactants at the electrode/electrolyte double layer. The half-hour electrolysis and EIS were performed on Pb foil (2 cm^2) at −1.20 V_{RHE}.

concentration of corresponding substrates. It is noteworthy that our kinetic fittings are unlikely to be limited by the external mass transport of furfural for its surface adsorption[44] because excessive furfural was used in the electrolyte than the estimated saturated surface coverage of furfural (Supporting information note 3), and relatively low furfural conversions (<50%) were obtained in all measurements. These above kinetic differences agreed well with the hypothesis that was proposed from the isotopic studies and supported the possible different reaction pathways for FA and MF.

In summary of the electrokinetic studies, the furfural-to-FA conversion followed an L−H pathway, which required the adsorbed furfural to couple with the adsorbed H. The RDS in this pathway is the proton-coupled electron transfer (PCET) step. In contrast, the furfural-to-MF conversion followed an E−R pathway, with adsorbed furfural directly coupled with the adjacent protons in the electrolyte, which required strongly acidic conditions for C−O scission. Its formation included the RDS of first-electron transfer (ET) followed by the direct proton transfer.

Tailoring the Electrode−Electrolyte Interface with Cations and Correlating with Microenvironments. To further investigate the above-observed different roles of H_2O and H_3O^+ at the interfacial regions, we tailored the microenvironments using quaternary alkyl ammonium cations. These cationic species with their tunable hydrophobic alkyl chains occupy the negatively charged electrode interface (either randomly or regularly) within the outer Helmholtz plane (OHP) due to electrostatic attraction,[44,45] thus altering the electron-transfer dynamics via concurrently modified interfacial enviroments,[46] including local chemical (e.g., local pH and H_2O) and physical (e.g., capacitance and electric filed) properties. Herein, we used a series of quaternary alkyl ammonium cations with symmetric carbon chains, namely, methyl$_4$N$^+$ (C4), ethyl$_4$N$^+$ (C8), propyl$_4$N$^+$ (C12), and butyl$_4$N$^+$ (C16). These cationic surfactants can systematically manipulate interfacial properties, benefiting from their tunable radius with varying alkyl chain lengths,[28] minimized interactions with reactants/products,[28,29,47] and excellent stability without structure changes under electrolysis conditions.[33] The restructuring of local environments was monitored through electrochemical characterizations (i.e., EIS) combined with mathematical modeling.

We conducted half-hour electrolysis at −1.20 V_{RHE} in the presence of cationic surfactants with varied chain lengths (from C4 to C16, Figure 4a region 2) and cationic concentrations (from 50 to 1000 mM, Figure 4a region 3) in the furfural containing electrolytes. The passed charges (right *y*-axis) were

https://doi.org/10.1021/acscatal.2c03163
ACS Catal. 2022, 12, 14072−14085

continuously decreased from 58.0 to 10.8C in the three regions of Figure 4a, which can be attributed to the site-blocking effects. That is, the presence of cationic surfactants in the electrolyte hindered the external mass transport of furfural and protons to the electrode surface for their subsequent adsorption. Interestingly, the FE of FA gradually increased from 14.2 to 25.5% in regions 1 and 2, followed by a continuous decline to 5.3% in region 3. In contrast, the FE of MF constantly dropped from 14.7 to 0.7% in regions 1 and 2. By further increasing the C16 concentration in region 3, MF was no longer produced. Over the whole regions, the FE of H_2 steadily decreased from 27.5 to 6.8%.

We then probed local ion distributions by EIS to quantitively relate product distribution to the modified electrode/electrolyte interface. EIS was carried out at the same potential of −1.20 V_{RHE} and other conditions to keep identical to the CA tests (Figure 4b). Double-layer capacitance (i.e., C_{dl}) represents a quantitative parameter to probe any changes at the interface. Interestingly, the trend of C_{dl} is consistent with that of FE of FA, showing an initial downward trend (regions 1 and 2) followed by an upward trend (region 3), with a minimum value of 32.53 μF cm^{-2} obtained at 50 mM C16-containing electrolytes. We then related the product distribution to the local concentration of H_2O and H_3O^+ at the electrode/electrolyte interface based on the formula of C_{dl} (inset of Figure 4b). As shown in Figure 4c, the decreased C_{dl} in the presence of cationic surfactants was due to the lowered dielectric constant (ε) resulting from their organic hydrophobic chains, as compared to the background ions in the aqueous electrolyte (region 1).[33,47] By further increasing the chain length from C4 to C16 in region 2, a continuous decrease in C_{dl} was observed as a result of the increased double-layer distance (d). This is because the cations with gradually enlarged molecular size arrange at the negatively biased electrode interface and replace positively charged H_3O^+ ions (thereby increasing local pH) with smaller size. As such, a sharp decrease in FE of MF was observed in region 2, highlighting the role of interfacial H_3O^+ in the furfural-to-MF pathway. Finally, when further increasing the concentration of C16 (region 3), a more compact cationic layer with a subsequently elevated C_{dl} is observed. From the Helmholtz model and Gouy−Chapman theory, as the electrolyte becomes more concentrated, there would be a more compressed diffuse layer (decreased d) and a consequent increase in capacitance.[48] Therefore, the intensively organized, large-sized cations with organic hydrophobic chains and high concentrations created a compact hydrophobic layer at the interface,[28] leading to the displaced and decreased local H_2O content. The disrupted interfacial water led to a gradual decrease in FE of FA in region 3, agreeing well with our expectations that H_2O is critical in the furfural-to-FA pathway. It also suggested that the formation of FA requires sufficient adsorbed H that sources from nearby water for the generation of FA through an L−H pathway. The unaffected FE of hydrofuoin in regions 1−2 and a gradual increase in its FE in region 3 can be attributed to the outer-sphere feature of hydrofuroin formation, which is independent of the inner sphere route for FA and MF generations. As a general rule of thumb, double-layer capacitance is largely independent on the nature of the electrode surface and the type of ions in solution.[48] Some control experiments were performed to exclude other possible interferences, including surface morphology (Figure S26a,b), roughness of the electrode (Figure S26c,e), and cationic structures and anion types of those surfactants (Figure S27).

We further quantitively estimated local pH changes that tune selectivity. The FE of product as a function of H_3O^+ concentration (bulk pH) without cationic surfactants was first examined by half-hour electrolysis at −1.20 V_{RHE}. The electrolyte was kept at a constant ionic strength (total concentration of H_3O^+ and Na^+ of 0.5 M) with varied bulk pH by adjusting the relative ratio of H_3O^+ and Na^+. As shown in Figure 5a, a systematic decrease in the percentage of MF [MF%, defined as the FE percentage of MF/(MF+FA) in %] was observed with the increase in bulk pH. The corresponding FE−pH curve shows that MF% decreased exponentially from 55.50 to 2.11 as the bulk pH increased from ∼0 to 1.7 (H_3O^+ concentration decreasing from 0.5 to 0.02 M), in agreement with the pH sensitivity in furfural-to-MF conversion. If we assume the addition of those cations displaced local positively charged H_3O^+,[39,49,50] which mainly contributed to the changes in MF selectivity, we can then estimate the local pH change (ΔpH) in the presence of cationic surfactants based on the varied MF%. With the addition of C4-C16 to the pH 0 electrolyte (the experimentally tested bulk pH of around 0 maintained), the local ΔpH was calculated to be varied from 0.79−1.67. This means that at the same bulk pH of 0, after local pH elevation of 1.67 (Figure 5 purple dot), the MF% has drastically decreased from 55.50% to only 2.56% (over 20 times decrease), highlighting the dramatic influence of interfacial pH on the MF formation pathway. Additionally, based on the local ΔpH estimation, we further used a model based on the Gouy−Chapman−Stern (GCS) theory and built the local ΔpH−electric field− product selectivity relationships

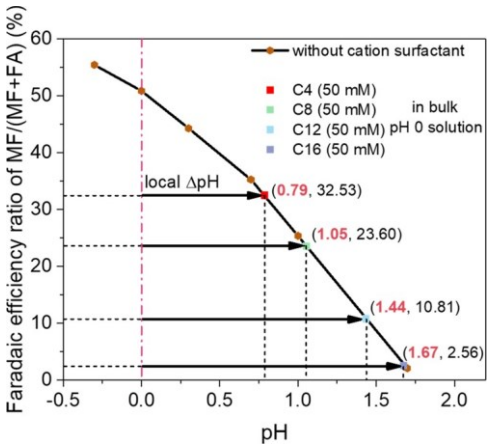

Figure 5. Faradaic efficiency (FE) percentage of MF/(MF + FA) at different pHs in estimating local pH and its correlation with product selectivity through tailoring the double layer. The results shown in orange dots and the black line were performed at the electrolytes without cationic surfactants. To adjust electrolyte pH while maintaining a constant ionic strength at 0.5 M, we used different ratios of H_2SO_4/Na_2SO_4. The four dots on the black curve with different colors are the FE percentage for four cationic surfactant-containing electrolytes, calculated from Figure 4a region 2. 50 mM cationic surfactants were added to the electrolyte with 0.5 M H_2SO_4 and 1:3 (v/v) CH_3CN/H_2O as cosolvent (H−only electrolyte). ΔpH is calculated from the pH change as compared to the electrolysis results with or without cationic surfactants. Electrolysis was conducted on Pb foil for 0.5 h at −1.20 V_{RHE}.

https://doi.org/10.1021/acscatal.2c03163
ACS Catal. 2022, 12, 14072−14085

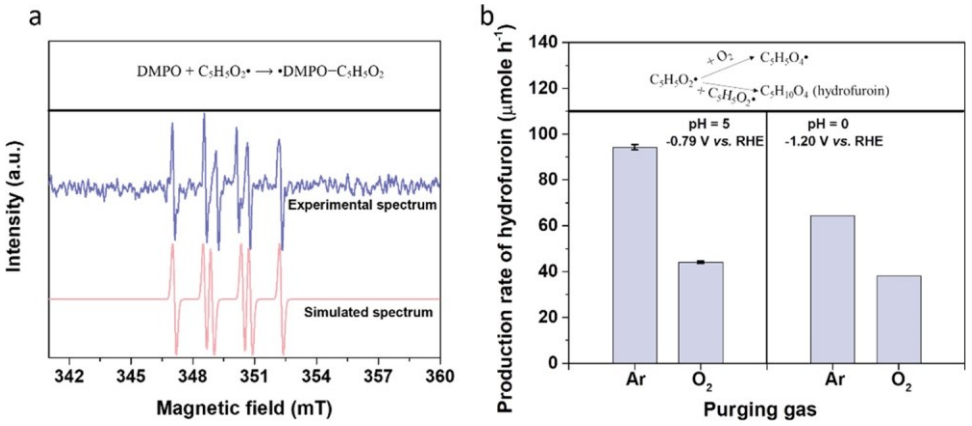

Figure 6. Capturing free radicals during hydrofuroin formation. (a) Experimental and simulated EPR spectra were instantly obtained after 1 h electrolysis on Pb foil at −0.79 V_{RHE}. The electrolysis was performed on Pb foil in pH 5 buffer solution with 20 mM furfural dissolved in 1:3 (v/v) CH_3CN/H_2O cosolvent. 30 mg of DMPO as a spin trapper was added to the electrolyte after 5 min of the electrolysis. (b) Comparison of the production rate of hydrofuroin between Ar and O_2 as the purging gas (100 mL min^{-1}) for 1 h electrolysis with 20 mM furfural. The electrolysis was performed in pH 5 and pH 0 solutions with 1:3 (v/v) CH_3CN/H_2O as cosolvent at −0.79 and −1.20 V_{RHE}, respectively.

(detailed in the Supporting information note 4 and Figure S28).

Taken all together, through tailoring the double layer, we have related product selectivity to local pH or interfacial electric field and acquired deeper insights into the influence of local proton concentration at the electrode−electrolyte interface, instead of that in the bulk electrolyte regions. These results further suggested that microenvironments (e.g., H_3O^+ and H_2O content) are indeed critical in the ECH pathways toward MF and FA.

Mechanism of Hydrofuroin Formation. Hydrofuroin as a dimeric product was suggested to be generated from two possible processes in previous works: a complete surface reaction of self-coupling of two adsorbed ketyl radicals[18] and a fully outer-sphere route in the solution phase that is independent of the surface properties.[14] The ketyl radicals were identified as the critical intermediate in either pathway, but no direct evidence has indicated its generation on the surface or in the solution so far. Here, we combined experimental and computational tools to elucidate its detailed formation mechanism.

We implemented EPR spectroscopy and oxygen inhibition reaction (OIR) for capturing free radicals (i.e., furan radicals) in the electrolyte. Because of the transient presence of free radicals in the electrolyte, 5,5-dimethyl-1-pyrroline N-oxide (DMPO) was added to react with free radicals to form spin adducts that can be detected by EPR.[51] To increase EPR intensity, the electrolysis was conducted in a pH 5 buffer solution at −0.79 V_{RHE} for 1 h to ensure a high hydrofuroin selectivity (Figure S23). DMPO was added to the electrolyte after 5 min of the reaction was initiated. The obtained EPR signal with six peaks agreed well with the simulated spectra of the desired spin adduct $^{\cdot}DMPO-C_5H_5O_2$ (Figure 6a), which indeed suggested the existence of furan radicals in the electrolyte during furfural reduction. The addition of DMPO was believed not to alter the dynamics of $C_5H_5O_2^{\cdot}$ radical formation routes, as a similar approach of detecting free radicals has been adopted in other electrochemical transformations, such as nitrate reduction[52] and chain reactions among furan derivatives.[53] Furthermore, OIR experiments using O_2 provide another proof in the presence of free radicals in the electrolyte. Molecular O_2 with two unpaired electrons in its separate orbitals can react with the free radicals ($C_5H_5O_2^{\cdot}$) to form peroxyl radicals ($C_5H_5O_4^{\cdot}$),[54,55] and thus, the self-combination of two $C_5H_5O_2^{\cdot}$ in the formation of dimeric hydrofuroin would be inhibited. Indeed, Figure 6b shows that the production rate of hydrofuroin appreciably decreased from 94.3 ± 1.2 to 44.1 ± 0.6 μmole h^{-1}, after changing the purging gas from Ar to O_2 (100 mL min^{-1}) during 1 h electrolysis at pH 5. It should be noted that we have detected the O_2 concentration of 0.92 mM by the Winkler method,[41] which was sufficient to combine with free radicals in the electrolyte, with detailed quantification and analysis shown in Supporting Information methods. These results suggested that the free radicals were indeed formed and diffused to the bulk electrolyte for their transient presence and self-coupling, which also explained the absence of signal for coupled C−C surface intermediate from *in situ* FTIR in previous work.[18] The obtained dimer formation mechanisms by self-coupling of two free radicals could be extended to similar compounds with aldehyde groups, such as HMF[12,56] and benzaldehyde.[17]

Although free radicals were experimentally detected in the electrolyte, it is still unable to determine whether they are formed by the first H addition on the surface (forming furfural-H*) followed by their desorption or they are directly generated in the solution phase. In addition, in a wide pH range (3−11, Figure S23), we have observed an inverse trend between hydrofuroin and FA formations and an unfavorable furfural-to-hydrofuroin conversion at more negative potentials, suggesting the possible competitive pathways between hydrofuroin and FA. However, it is still unclear whether the production routes of hydrofuroin and FA are bifurcated from a common adsorbate intermediate (e.g., furfural-H*) or they are completely independent pathways.

DFT Computations. To address the above questions, we performed density functional theory (DFT) calculations in VASP[57,58] (PAW-PBE,[59,60] DFT-D3,[61] see Supporting Information for details) to explore key mechanistic insights proposed by our experiments. We evaluated the potential-dependent[62] Gibbs free energies (ΔG) of elementary steps, additionally calculating activation free energies (ΔG_{act}) for selected key steps; energetics are provided in Figure 7 and Table S13 and S14. We present our DFT calculations based on representative experimental conditions of pH = 0 and U =

https://doi.org/10.1021/acscatal.2c03163
ACS Catal. 2022, 12, 14072−14085

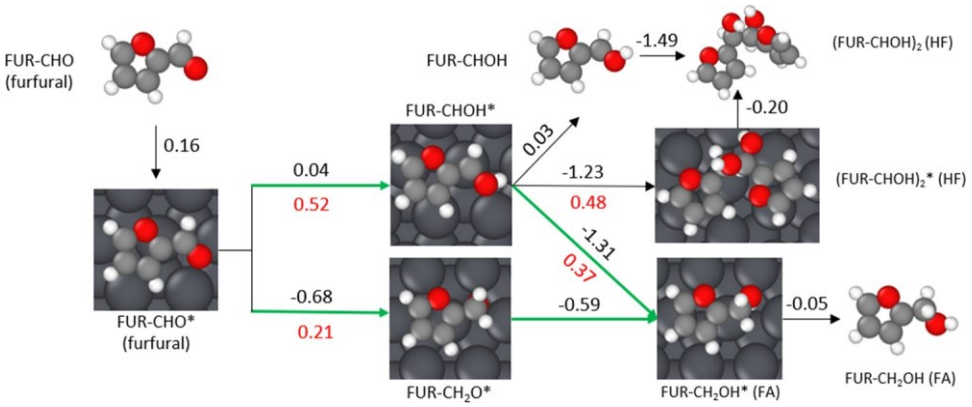

Figure 7. Calculated reaction energetics for furfural hydrogenation on Pb(111) at −0.55 V_{RHE}. For each elementary step, ΔG_{act} (activation free energy, eV) is marked red and ΔG (reaction free energy, eV) is marked black. In species naming, FUR denotes the furan ring, and * denotes an adsorbed species. Atoms are colored as follows: O (red), C (gray), H (white), Pb (dark gray). Electrochemical steps (those involving a H^+/e^- transfer) are shown with green arrows; nonelectrochemical steps are shown with black arrows.

−0.55 V_{RHE}, assuming that H_3O^+ is the proton source for the reaction. Although we do not explicitly calculate any barriers of H_3O^+ dissociation, we note that previous work[63] has shown it is negligible ($E_a \sim 0.08$ eV) relative to the other calculated barriers and therefore believe our implicit treatment of these effects is appropriate.[64] We chose the Pb(111) surface as a catalyst model given our experimental evidence that Pb is in its metallic state (Figure S17). We note that the (111) facet was selected in lieu of a detailed study of possible active facets, which may include other surface types. We have not explicitly accounted for solvent effects, contributions from counterions and the electrical double layer, surface charge effects, or coverage effects (including effects of adsorbed ions or surface solvation by water[65]) in our surface calculations. While we acknowledge this may impact our conclusions, we note that recent work suggests some of these (e.g., charge gradient) may not affect the qualitative nature of our conclusions.[66] Our experimental results (Figure 3) suggest that the coverage by furfural and hydrogen is very small at our potential of interest (−0.55 V_{RHE}) though we note that these coverages may become more significant as potential becomes more negative (approaching −1.20 V_{RHE} in our experiments). Our results show that at low surface coverage, interactions between H* and other reaction intermediates may have negligible impacts on reaction-free energies (Table S15). The most stable adsorption geometries of all reaction intermediates are provided in Figure S29; these are consistent with previous literature.[67] We focus our analysis on (1) the formation of the critical ketyl radical species, which our computations suggest occurs as an outer-sphere electrochemical process; (2) the formation of hydrofuroin, which our computations suggest occurs via solution-phase coupling of ketyl radicals; and (3) the Pb(111) surface's favorability for FA formation relative to the formation of the ketyl radical or hydrofuroin.

Furfural adsorption is energetically uphill on the Pb(111) surface (ΔG = 0.16 eV relative to a gas-phase furfural reference). Once adsorbed, we considered two possible additions of proton−electron pairs to furfural, one on either side of the C=O bond (Figure 7). Our calculations showed that H* addition on the C of adsorbed furfural is significantly more favorable (ΔG_{act} = 0.21, ΔG = −0.68 eV at −0.55 V_{RHE}) than the corresponding addition to O (ΔG_{act} = 0.52, ΔG = 0.04 eV). This suggests that the formation of the ketyl radical, a key intermediate identified experimentally, from surface-bound furfural is relatively unfavorable. We evaluated the solution-phase reaction energetics (using Gaussian 09,[68−70] detailed in Supporting Information) to explore the possibility of direct formation of the ketyl radical from furfural in solution (Table S15). We calculated a ΔG of 0.23 eV for this process at −0.55 V_{RHE}, noting that the corresponding addition of H to the C atom (which is more favorable on the surface) had an unfavorable ΔG of 1.15 eV (Table S15). Together, these results suggest the likelihood of the ketyl radical forming in solution (i.e., as an outer-sphere step) rather than on the surface. We note a slight inconsistency in the thermodynamic cycle for the listed solution-phase elementary steps due to the direct comparison of solution-phase energetics (G09) with surface-mediated pathways utilizing gas-phase references (VASP). We anticipate that the true adsorption energies for furfural/radical adsorption are overestimated by our gas-phase reference (i.e., a solution-phase reference will be more stable, in accordance with recent work[71,72]), lending additional difficulty to furfural adsorption and hydrogenation relative to outer-sphere hydrogenation.

We additionally evaluated energetics for hydrofuroin formation from the ketyl radical (Figure 7). The direct coupling of ketyl radicals to form hydrofuroin is favorable (ΔG = −1.49 eV in gas phase/VASP, −1.55 eV in implicit solution/G09). We did not explicitly evaluate the activation energy of this process due to the relative complexity of obtaining a representative value in solution. The primary challenge with the solution-phase coupling is anticipated to be the collision frequency at the correct orientation in the three-dimensional context (in contrast with the two-dimensional surface). We also considered a surface-based coupling of ketyl radicals, particularly considering their adsorption (ΔG = −0.03 eV) is more favorable than that of furfural (ΔG = 0.16 eV). The surface coupling has a ΔG_{act} of 0.48 eV (ΔG of −1.23 eV). While this barrier is not insurmountable at room temperature, its relative difficulty makes it more likely that solution-phase coupling carries the majority of the reaction flux to form hydrofuroin.

Finally, our calculations suggest two possible surface mechanisms for the formation of FA. The ketyl radical identified previously as a key intermediate has a preference for the formation of FA (ΔG_{act} = 0.37 eV, ΔG = −1.31 eV) in comparison with HF (ΔG_{act} = 0.48 eV, ΔG = −1.23 eV); FA becomes more favored as the reaction potential becomes more

https://doi.org/10.1021/acscatal.2c03163
ACS Catal. 2022, 12, 14072−14085

Scheme 2. Summarized Reaction Pathways for Furfural Reduction toward Three Key Products: FA, MF, and Hydrofuroin[a]

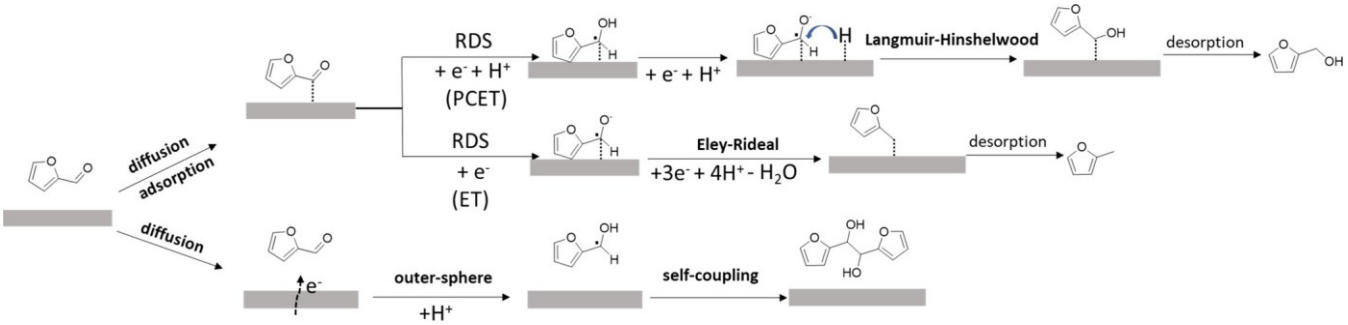

[a]This scheme summarizes the new insights acquired from this work, including the FA and MF formation pathways from experiments and the hydrofuroin formation pathways from both experiments and computation.

negative, as HF formation from the radical is not an electrochemical process. Additionally, as mentioned previously, the formation of a ketyl radical from adsorbed furfural (ΔG_{act} = 0.52, ΔG = 0.04 eV) is unfavorable in comparison with the hydrogenation of the carbonyl's C atom (ΔG_{act} = 0.21, ΔG = −0.68 eV). This suggests that any surface reactions of adsorbed furfural are funneled preferentially to FA. We are unable to elucidate the fine details of the potential-dependent product distribution in Figure 1b using our methodology discussed here, inferring that other complex factors such as solution-phase kinetics, potential-dependent coverage effects, or advanced mechanisms not considered here (e.g., proton shuttling) limit our ability to describe this behavior with our relatively simple model. Based on the understanding of the outer-sphere pathway for hydrofuroin production, we proposed to use a relatively inert cathode (i.e., carbon cloth) to suppress ECH and favor dimer formation pathways, because the outer-sphere route is independent of the surface property of the electrode. Indeed, as shown in Figure S30, we observed the hydrofuroin selectivity of 76% with a minimization of FA on hydrophilic carbon cloth at −0.80 V_{RHE}.

CONCLUSIONS

In summary, we have acquired deep understanding of the electrochemical reduction pathways of furfural toward the key products, i.e., FA, MF, and hydrofuroin, on Pb surfaces via tailoring the local environments (Scheme 2). H/D isotopic labeling and incorporation studies suggested that the product-selective and surface-property-dependent KIE was only exhibited for the formation of FA, but not MF, indicating the different RDS of hydrogen additions. Combined with electrokinetic studies, we have confirmed the critical roles of H_2O and H_3O^+ in the generation of FA and MF, respectively, and suggested the PCET and ET as the RDS for their respective production. Electrokinetic reaction order fittings further suggested L−H and E−R mechanisms for FA and MF productions, respectively. Through modifying the double layer by cations with large radii, we have correlated their selective pathways with the local chemical and physical properties.

Finally, as suggested by EPR, OIR, and DFT calculations, hydrofuroin is formed through the outer-sphere generation of ketyl radicals followed by their self-coupling in the solution phase, independent of the surface properties of electrodes. The mechanistic insights obtained in our work can potentially be extended to a wide range of intriguing organic compounds with the aldehyde group (e.g., HMF and benzaldehyde). Apart from designing electrode materials or developing reactors to alter reaction pathways and increase reaction kinetics, our work provided additional reaction dimensions in adjusting the local environments to optimize the electrochemical transformations. The experimental methods herein are transferable to other electrochemical reactions (electroreduction of water, CO_2, nitrate, etc.) and will provide complementary information when combined with *in situ* surface characterization techniques to elucidate the reaction mechanisms in future studies.

ASSOCIATED CONTENT

Supporting Information

The Supporting Information is available free of charge at https://pubs.acs.org/doi/10.1021/acscatal.2c03163.

Experimental details; 1H NMR and GC-MS results; isotopic incorporation studies details; physical characterization of electrodes; derivative equations for L−H and E−R pathways; mathematic modeling of double layers; and geometries of considered reaction intermediates and calculated free energy for DFT (PDF)

AUTHOR INFORMATION

Corresponding Authors

Luke T. Roling − *Department of Chemical and Biological Engineering, Iowa State University, Ames, Iowa 50011, United States;* orcid.org/0000-0001-9742-2573; Email: roling@iastate.edu

Wenzhen Li − *Department of Chemical and Biological Engineering, Iowa State University, Ames, Iowa 50011, United States;* orcid.org/0000-0002-1020-5187; Email: wzli@iastate.edu

Authors

Hengzhou Liu − *Department of Chemical and Biological Engineering, Iowa State University, Ames, Iowa 50011, United States*

Deep M. Patel − *Department of Chemical and Biological Engineering, Iowa State University, Ames, Iowa 50011, United States*

Yifu Chen − *Department of Chemical and Biological Engineering, Iowa State University, Ames, Iowa 50011, United States*

Jungkuk Lee − *Department of Chemical and Biological Engineering, Iowa State University, Ames, Iowa 50011, United States*

Ting-Han Lee − *Department of Chemical and Biological Engineering, Iowa State University, Ames, Iowa 50011, United States;* orcid.org/0000-0002-5531-052X
Sarah D. Cady − *Department of Chemistry, Iowa State University, Ames, Iowa 50011, United States*
Eric W. Cochran − *Department of Chemical and Biological Engineering, Iowa State University, Ames, Iowa 50011, United States;* orcid.org/0000-0003-3931-9169

Complete contact information is available at: https://pubs.acs.org/10.1021/acscatal.2c03163

Notes

The authors declare no competing financial interest.

ACKNOWLEDGMENTS

This work was supported by the NSF through CBET-1947435. W.L. is grateful to his Herbert L. Stiles Professor Fellowship and support from USDA-NIFA (20216702134650) and the IEC competitive fund (20-IEC-019). The authors thank Drs. Warren E. Straszheim and Carolina Selvati for their assistance with XRD measurements. The authors also acknowledge Prof. Brent H. Shanks, Dr. Yan Cheng, and Hsi-Hsin Lin for their help in GC-MS tests, and Prof. Jean-Philippe Tessonnier for fruitful discussion on electrochemical reduction of furfural.

REFERENCES

(1) Lucas, F. W. S.; Grim, R. G.; Tacey, S. A.; Downes, C. A.; Hasse, J.; Roman, A. M.; Farberow, C. A.; Schaidle, J. A.; Holewinski, A. Electrochemical Routes for the Valorization of Biomass-Derived Feedstocks: From Chemistry to Application. *ACS Energy Lett.* 2021, *6*, 1205−1270.

(2) Akhade, S. A.; Singh, N.; Gutiérrez, O. Y.; Lopez-Ruiz, J.; Wang, H.; Holladay, J. D.; Liu, Y.; Karkamkar, A.; Weber, R. S.; Padmaperuma, A. B.; et al. Electrocatalytic hydrogenation of biomass-derived organics: a review. *Chem. Rev.* 2020, *120*, 11370−11419.

(3) Luo, H.; Barrio, J.; Sunny, N.; Li, A.; Steier, L.; Shah, N.; Stephens, I. E.; Titirici, M. M. Progress and Perspectives in Photo-and Electrochemical-Oxidation of Biomass for Sustainable Chemicals and Hydrogen Production. *Adv. Energy Mater.* 2021, *11*, No. 2101180.

(4) Bozell, J. J.; Petersen, G. R. Technology development for the production of biobased products from biorefinery carbohydrates—the US Department of Energy's "Top 10" revisited. *Green Chem.* 2010, *12*, 539−554.

(5) Du, L.; Shao, Y.; Sun, J.; Yin, G.; Du, C.; Wang, Y. Electrocatalytic valorisation of biomass derived chemicals. *Catal. Sci. Technol.* 2018, *8*, 3216−3232.

(6) Gandini, A.; Belgacem, M. N. Furans in polymer chemistry. *Prog. Polym. Sci.* 1997, *22*, 1203−1379.

(7) Moreau, C.; Belgacem, M. N.; Gandini, A. Recent catalytic advances in the chemistry of substituted furans from carbohydrates and in the ensuing polymers. *Top Catal.* 2004, *27*, 11−30.

(8) Wang, L.; Chen, E. Y.-X. Recyclable supported carbene catalysts for high-yielding self-condensation of furaldehydes into C10 and C12 furoins. *ACS Catal.* 2015, *5*, 6907−6917.

(9) Shang, X.; Yang, Y.; Sun, Y. Electrohydrodimerization of biomass-derived furfural generates a jet fuel precursor. *Green Chem.* 2020, *22*, 5395−5401.

(10) May, A. S.; Biddinger, E. J. Strategies to control electrochemical hydrogenation and hydrogenolysis of furfural and minimize undesired side reactions. *ACS Catal.* 2020, *10*, 3212−3221.

(11) Brosnahan, J. T.; Zhang, Z.; Yin, Z.; Zhang, S. Electrocatalytic reduction of furfural with high selectivity to furfuryl alcohol using AgPd alloy nanoparticles. *Nanoscale* 2021, *13*, 2312−2316.

(12) Liu, H.; Lee, T.-H.; Chen, Y.; Cochran, E. W.; Li, W. Paired electrolysis of 5-(hydroxymethyl) furfural in flow cells with a high-performance oxide-derived silver cathode. *Green Chem.* 2021, *23*, 5056−5063.

(13) Bharath, G.; Banat, F. High-Grade Biofuel Synthesis from Paired Electrohydrogenation and Electrooxidation of Furfural Using Symmetric Ru/Reduced Graphene Oxide Electrodes. *ACS Appl. Mater. Interfaces.* 2021, *13*, 24643−24653.

(14) Chadderdon, X. H.; Chadderdon, D. J.; Matthiesen, J. E.; Qiu, Y.; Carraher, J. M.; Tessonnier, J.-P.; Li, W. Mechanisms of furfural reduction on metal electrodes: Distinguishing pathways for selective hydrogenation of bioderived oxygenates. *J. Am. Chem. Soc.* 2017, *139*, 14120−14128.

(15) Allen, J. B.; Larry, R. F.*Electrochemical Methods Fundamentals and Applications*; John Wiley & Sons, 2001; pp 624−625.

(16) He, Z. D.; Chen, Y. X.; Santos, E.; Schmickler, W. The Pre−exponential Factor in Electrochemistry. *Angew. Chem., Int. Ed.* 2018, *57*, 7948−7956.

(17) Andrews, E.; Lopez-Ruiz, J. A.; Egbert, J. D.; Koh, K.; Sanyal, *U.*; Song, M.; Li, D.; Karkamkar, A. J.; Derewinski, M. A.; Holladay, J.; et al. Performance of base and noble metals for electrocatalytic hydrogenation of bio-oil-derived oxygenated compounds. *ACS Sustainable Chem. Eng.* 2020, *8*, 4407−4418.

(18) Anibal, J.; Xu, B. Electroreductive C−C Coupling of Furfural and Benzaldehyde on Cu and Pb Surfaces. *ACS Catal.* 2020, *10*, 11643−11653.

(19) Waegele, M. M.; Gunathunge, C. M.; Li, J.; Li, X. How cations affect the electric double layer and the rates and selectivity of electrocatalytic processes. *J. Chem. Phys.* 2019, *151*, No. 160902.

(20) Lin, Y.; Deng, C.; Wu, L.; Zhang, Y.; Chen, C.; Ma, W.; Zhao, J. Quantitative isotope measurements in heterogeneous photocatalysis and electrocatalysis. *Energy Environ. Sci.* 2020, *13*, 2602−2617.

(21) Lum, Y.; Ager, J. W. Evidence for product-specific active sites on oxide-derived Cu catalysts for electrochemical CO_2 reduction. *Nat. Catal.* 2019, *2*, 86−93.

(22) Lum, Y.; Cheng, T.; Goddard, W. A., III; Ager, J. W. Electrochemical CO reduction builds solvent water into oxygenate products. *J. Am. Chem. Soc.* 2018, *140*, 9337−9340.

(23) Dunwell, M.; Lu, Q.; Heyes, J. M.; Rosen, J.; Chen, J. G.; Yan, Y.; Jiao, F.; Xu, B. The central role of bicarbonate in the electrochemical reduction of carbon dioxide on gold. *J. Am. Chem. Soc.* 2017, *139*, 3774−3783.

(24) Chang, X.; Malkani, A.; Yang, X.; Xu, B. Mechanistic Insights into Electroreductive C−C coupling between CO and acetaldehyde into multicarbon products. *J. Am. Chem. Soc.* 2020, *142*, 2975−2983.

(25) Zhang, Y.; Zhang, H.; Liu, A.; Chen, C.; Song, W.; Zhao, J. Rate-limiting O−O bond formation pathways for water oxidation on hematite photoanode. *J. Am. Chem. Soc.* 2018, *140*, 3264−3269.

(26) Tse, E. C. M.; Varnell, J. A.; Hoang, T. T.; Gewirth, A. A. Elucidating proton involvement in the rate-determining step for Pt/Pd-based and non-precious-metal oxygen reduction reaction catalysts using the kinetic isotope effect. *J. Phys. Chem. Lett.* 2016, *7*, 3542−3547.

(27) Yang, X.; Nash, J.; Anibal, J.; Dunwell, M.; Kattel, S.; Stavitski, E.; Attenkofer, K.; Chen, J. G.; Yan, Y.; Xu, B. Mechanistic insights into electrochemical nitrogen reduction reaction on vanadium nitride nanoparticles. *J. Am. Chem. Soc.* 2018, *140*, 13387−13391.

(28) Li, J.; Li, X.; Gunathunge, C. M.; Waegele, M. M. Hydrogen bonding steers the product selectivity of electrocatalytic CO reduction. *Proc. Natl. Acad. Sci. U.S.A.* 2019, *116*, 9220−9229.

(29) Banerjee, S.; Han, X.; Thoi, V. S. Modulating the electrode−electrolyte interface with cationic surfactants in carbon dioxide reduction. *ACS Catal.* 2019, *9*, 5631−5637.

(30) Goyal, A.; Koper, M. T. The Interrelated Effect of Cations and Electrolyte pH on the Hydrogen Evolution Reaction on Gold Electrodes in Alkaline Media. *Angew. Chem., Int. Ed.* 2021, *60*, 13452−13462.

(31) Singh, M. R.; Kwon, Y.; Lum, Y.; Ager, J. W., III; Bell, A. T. Hydrolysis of electrolyte cations enhances the electrochemical reduction of CO2 over Ag and Cu. *J. Am. Chem. Soc.* 2016, *138*, 13006−13012.

(32) Huang, B.; Rao, R. R.; You, S.; Hpone Myint, K.; Song, Y.; Wang, Y.; Ding, W.; Giordano, L.; Zhang, Y.; Wang, T.; et al. Cation- and pH-Dependent Hydrogen Evolution and Oxidation Reaction Kinetics. *JACS Au* 2021, *1*, 1674−1687.
(33) Sarkar, S.; Maitra, A.; Banerjee, S.; Thoi, V. S.; Dawlaty, J. M. Electric Fields at Metal−Surfactant Interfaces: A Combined Vibrational Spectroscopy and Capacitance Study. *J. Phys. Chem. B* 2020, *124*, 1311−1321.
(34) Ryu, J.; Surendranath, Y. Tracking electrical fields at the Pt/H2O interface during hydrogen catalysis. *J. Am. Chem. Soc.* 2019, *141*, 15524−15531.
(35) Intikhab, S.; Rebollar, L.; Li, Y.; Pai, R.; Kalra, V.; Tang, M. H.; Snyder, J. D. Caffeinated interfaces enhance alkaline hydrogen electrocatalysis. *ACS Catal.* 2020, *10*, 6798−6802.
(36) Jung, S.; Biddinger, E. J. Electrocatalytic hydrogenation and hydrogenolysis of furfural and the impact of homogeneous side reactions of furanic compounds in acidic electrolytes. *ACS Sustainable Chem. Eng.* 2016, *4*, 6500−6508.
(37) Jung, S.; Karaiskakis, A. N.; Biddinger, E. J. Enhanced activity for electrochemical hydrogenation and hydrogenolysis of furfural to biofuel using electrodeposited Cu catalysts. *Catal. Today* 2019, *323*, 26−34.
(38) Lohr, T. L.; Li, Z.; Marks, T. J. Thermodynamic strategies for C−O bond formation and cleavage via tandem catalysis. *Acc. Chem. Res.* 2016, *49*, 824−834.
(39) Ryu, J.; Wuttig, A.; Surendranath, Y. Quantification of Interfacial pH Variation at Molecular Length Scales Using a Concurrent Non-Faradaic Reaction. *Angew. Chem., Int. Ed.* 2018, *57*, 9300−9304.
(40) Seifitokaldani, A.; Gabardo, C. M.; Burdyny, T.; Dinh, C.-T.; Edwards, J. P.; Kibria, M. G.; Bushuyev, O. S.; Kelley, S. O.; Sinton, D.; Sargent, E. H. Hydronium-induced switching between CO_2 electroreduction pathways. *J. Am. Chem. Soc.* 2018, *140*, 3833−3837.
(41) Lopez-Ruiz, J. A.; Sanyal, U.; Egbert, J.; Gutiérrez, O. Y.; Holladay, J. Kinetic investigation of the sustainable electrocatalytic hydrogenation of benzaldehyde on Pd/C: effect of electrolyte composition and half-cell potentials. *ACS Sustainable Chem. Eng.* 2018, *6*, 16073−16085.
(42) Singh, N.; Sanyal, U.; Ruehl, G.; Stoerzinger, K. A.; Gutiérrez, O. Y.; Camaioni, D. M.; Fulton, J. L.; Lercher, J. A.; Campbell, C. T. Aqueous phase catalytic and electrocatalytic hydrogenation of phenol and benzaldehyde over platinum group metals. *J. Catal.* 2020, *382*, 372−384.
(43) Schreier, M.; Yoon, Y.; Jackson, M. N.; Surendranath, Y. Competition between H and CO for active sites governs copper-mediated electrosynthesis of hydrocarbon fuels. *Angew. Chem.* 2018, *130*, 10378−10382.
(44) Dunwell, M.; Luc, W.; Yan, Y.; Jiao, F.; Xu, B. Understanding surface-mediated electrochemical reactions: CO_2 reduction and beyond. *ACS Catal.* 2018, *8*, 8121−8129.
(45) Orazem, M. E.; Tribollet, B. Electrochemical impedance spectroscopy. *New Jersey* 2008, 383−389.
(46) Pérez-Gallent, E.; Marcandalli, G.; Figueiredo, M. C.; Calle-Vallejo, F.; Koper, M. T. Structure-and potential-dependent cation effects on CO reduction at copper single-crystal electrodes. *J. Am. Chem. Soc.* 2017, *139*, 16412−16419.
(47) Banerjee, S.; Zhang, Z.-Q.; Hall, A. S.; Thoi, V. S. Surfactant Perturbation of Cation Interactions at the Electrode−Electrolyte Interface in Carbon Dioxide Reduction. *ACS Catal.* 2020, *10*, 9907−9914.
(48) Aikens, D.*Electrochemical Methods, Fundamentals and Applications*; ACS Publications, 1983; pp 534−577.
(49) Henckel, D. A.; Counihan, M. J.; Holmes, H. E.; Chen, X.; Nwabara, U. O.; Verma, S.; Rodríguez-López, J.; Kenis, P. J.; Gewirth, A. A. Potential dependence of the local pH in a CO2 reduction electrolyzer. *ACS Catal.* 2021, *11*, 255−263.
(50) Lu, X.; Zhu, C.; Wu, Z.; Xuan, J.; Francisco, J. S.; Wang, H. In situ observation of the pH gradient near the gas diffusion electrode of CO2 reduction in alkaline electrolyte. *J. Am. Chem. Soc.* 2020, *142*, 15438−15444.
(51) Barbieriková, Z.; Dvoranová, D.; Brezová, V. Photoinduced transformation of glycerol in titania suspensions.(An EPR spin trapping study of radical intermediates). *Catal. Today* 2018, *313*, 106−113.
(52) Li, J.; Zhan, G.; Yang, J.; Quan, F.; Mao, C.; Liu, Y.; Wang, B.; Lei, F.; Li, L.; Chan, A. W.; et al. Efficient ammonia electrosynthesis from nitrate on strained ruthenium nanoclusters. *J. Am. Chem. Soc.* 2020, *142*, 7036−7046.
(53) Chen, R.; Yang, C.; Zhou, Z.; Haeffner, F.; Dersjant, A.; Dulock, N.; Dong, Q.; He, D.; Jin, J.; Zhao, Y.; et al. Electrochemically Triggered Chain Reactions for the Conversion of Furan Derivatives. *Angew. Chem.* 2021, *133*, 7612−7617.
(54) Ligon, S. C.; Husar, B.; Wutzel, H.; Holman, R.; Liska, R. Strategies to reduce oxygen inhibition in photoinduced polymerization. *Chem. Rev.* 2014, *114*, 557−589.
(55) Husár, B.; Ligon, S. C.; Wutzel, H.; Hoffmann, H.; Liska, R. The formulator's guide to anti-oxygen inhibition additives. *Prog. Org. Coat.* 2014, *77*, 1789−1798.
(56) Chadderdon, X. H.; Chadderdon, D. J.; Pfennig, T.; Shanks, B. H.; Li, W. Paired electrocatalytic hydrogenation and oxidation of 5-(hydroxymethyl) furfural for efficient production of biomass-derived monomers. *Green Chem.* 2019, *21*, 6210−6219.
(57) Kresse, G.; Furthmüller, J. Efficient iterative schemes for ab initio total-energy calculations using a plane-wave basis set. *Phys. Rev. B* 1996, *54*, 11169.
(58) Kresse, G.; Furthmuller, J. Efficiency of ab-initio total energy calculations for metals and semiconductors using a plane-wave basis set. *Comput. Mater. Sci.* 1996, *6*, 15−50.
(59) Perdew, J. P.; Chevary, J. A.; Vosko, S. H.; Jackson, K. A.; Pederson, M. R.; Singh, D. J.; Fiolhais, C. Atoms, molecules, solids, and surfaces: Applications of the generalized gradient approximation for exchange and correlation. *Phys. Rev. B* 1992, *46*, 6671.
(60) Perdew, J. P.; Burke, K.; Ernzerhof, M. Generalized gradient approximation made simple. *Phys. Rev. Lett.* 1996, *77*, 3865.
(61) Grimme, S.; Antony, J.; Ehrlich, S.; Krieg, H. A consistent and accurate ab initio parametrization of density functional dispersion correction (DFT-D) for the 94 elements H-Pu. *J. Chem. Phys.* 2010, *132*, No. 154104.
(62) Nørskov, J. K.; Rossmeisl, J.; Logadottir, A.; Lindqvist, L.; Kitchin, J. R.; Bligaard, T.; Jonsson, H. Origin of the overpotential for oxygen reduction at a fuel-cell cathode. *J. Phys. Chem. B* 2004, *108*, 17886−17892.
(63) Yu, Q.; Bowman, J. M. Ab initio potential for $H_3O^+ \rightarrow H^+ + H_2O$: A step to a many-body representation of the hydrated proton? *J. Chem. Theory Comput.* 2016, *12*, 5284−5292.
(64) Akhade, S. A.; Bernstein, N. J.; Esopi, M. R.; Regula, M. J.; Janik, M. J. A simple method to approximate electrode potential-dependent activation energies using density functional theory. *Catal. Today* 2017, *288*, 63−73.
(65) Greeley, J.; Rossmeisl, J.; Hellmann, A.; Norskov, J. Theoretical trends in particle size effects for the oxygen reduction reaction. *Z. Phys. Chem.* 2007, *221*, 1209−1220.
(66) Li, J.; Stenlid, J. H.; Ludwig, T.; Lamoureux, P. S.; Abild-Pedersen, F. Modeling potential-dependent electrochemical activation barriers: revisiting the alkaline hydrogen evolution reaction. *J. Am. Chem. Soc.* 2021, *143*, 19341−19355.
(67) Shan, N.; Hanchett, M. K.; Liu, B. Mechanistic insights evaluating Ag, Pb, and Ni as electrocatalysts for furfural reduction from first-principles methods. *J. Phys. Chem. C* 2017, *121*, 25768−25777.
(68) Frisch, M. J.; Clemente, F.; Trucks, G. W.; Schlegel, H. B.; Scuseria, G. E.; Robb, M. A.; Cheeseman, J. R.; Scalmani, G.; Barone, V.; Mennucci, B.; Petersson, G. A.; Nakatsuji, H.; Caricato, M.; Li, X.; Hratchian, H. P.; Izmaylov, A. F.; Bloino, J.; Janesko, B. G.*Gaussian 09*, revision a. 01, 2009, pp 2044.
(69) Miertuš, S.; Scrocco, E.; Tomasi, J. Electrostatic interaction of a solute with a continuum. A direct utilizaion of AB initio molecular

potentials for the prevision of solvent effects. *Chem. Phys.* 1981, *55*, 117−129.
(70) Krishnan, R.; Binkley, J. S.; Seeger, R.; Pople, J. A. Self-consistent molecular orbital methods. XX. A basis set for correlated wave functions. *J. Chem. Phys.* 1980, *72*, 650−654.
(71) Akinola, J.; Campbell, C. T.; Singh, N. Effects of solvents on adsorption energies: a general bond-additivity model. *J. Phys. Chem. C* 2021, *125*, 24371−24380.
(72) Barth, I.; Akinola, J.; Lee, J.; Gutiérrez, O. Y.; Sanyal, U.; Singh, N.; Goldsmith, B. R. Explaining the structure sensitivity of Pt and Rh for aqueous-phase hydrogenation of phenol. *J. Chem. Phys.* 2022, *156*, No. 104703.

https://doi.org/10.1021/acscatal.2c03163
ACS Catal. 2022, 12, 14072−14085